



Subject Areas:

35B36, 35B35, 35B32, 35B25, 92C15

Keywords:

bulk-membrane coupled system, quorum and diffusion sensing, bifurcation, Green's function, synchrony, spikes

Author for correspondence:

M. J. Ward

e-mail: ward@math.ubc.ca

Pattern Forming Systems Coupling Linear Bulk Diffusion to Dynamically Active Membranes or Cells

D. Gomez, S. Iyaniwura, F.

Paquin-Lefebvre, and M. J. Ward

Dept. of Mathematics, UBC, Vancouver, BC, Canada

Some analytical and numerical results are presented for pattern formation properties associated with novel types of reaction-diffusion (RD) systems that involve the coupling of bulk diffusion in the interior of a multi-dimensional spatial domain to nonlinear processes that occur either on the domain boundary or within localized compartments that are confined within the domain. The class of bulk-membrane system considered herein is derived from an asymptotic analysis in the limit of small thickness of a thin domain that surrounds the bulk medium. When the bulk domain is a 2-D disk, a weakly nonlinear analysis is used to characterize Turing and Hopf bifurcations that can arise from the linearization around a radially symmetric, but spatially non-uniform, steady-state of the bulk-membrane system. In a different parameter regime, the existence and linear stability of localized membrane-bound spike patterns is analyzed for a Gierer-Meinhardt activator-inhibitor model that includes bulk coupling. Finally, the emergence of collective intracellular oscillations is studied for a class of PDE-ODE bulk-cell model in a bounded 2-D domain that contains spatially localized, but dynamically active, circular cells that are coupled through a linear bulk diffusion field. Applications of such coupled bulk-membrane or bulk-cell systems to some biological systems are outlined, and some open problems in this area are discussed.

1. Introduction

Membrane-bound pattern formation problems, as initiated in [1], involve the coupling of a bulk diffusion field in a bounded domain to a nonlinear reaction-diffusion (RD) system that is restricted to the domain boundary. Many

such bulk-membrane coupled RD systems are inspired by applications in cell biology owing to the natural compartmentalization of membrane-bound (surface) and cytosolic bulk species, as is typical in intracellular processes. Such models have been employed in the context of cell polarization (cf. [2–5]), which is the symmetry-breaking process leading to the spatial distribution of intracellular proteins into one or multiple clusters of molecules, and for which the persistence of such an asymmetric organization is known to be essential in the migration and development of cells (cf. [6]). Other applications include the dispersal and reformation of protein clusters resulting from pole-to-pole oscillatory dynamics of Min proteins in *E. Coli* (cf. [7,8]), which are needed for cell growth and division, as well as oscillatory dynamics of Cdc42 proteins in fission yeast (cf. [9]). While early mathematical models of the Min system incorporated the compartmentalization of Min proteins to the cell cytosol and membrane [7,10], more recent studies have been based on bulk-membrane coupled systems that directly model the interchange between bulk- and membrane-bound states of the Min proteins [11,12]. More recently, bulk-membrane RD systems have been used to model the clustering of proteins on the plasma membrane (cf. [13]) that arise from the coupling of the membrane to the cytoplasm. Such protein aggregates are believed to play a key role in various neurodegenerative diseases.

Previous studies of bulk-membrane coupled models have primarily focused on a combination of Turing-type linearized stability analysis and *in silico* experiments [1,2,14]. For both analysis and computation, bulk-membrane coupled systems introduce some unique challenges. In contrast to typical RD systems, bulk-membrane coupled models do not, in general, admit spatially homogeneous steady state solutions. Moreover, the coupling between bulk- and membrane-bound problems, as well as the curved geometry of the cell membrane lead to difficulties in numerical simulations. Both of these challenges have been addressed with the development of Turing-type stability analysis in which the linearization occurs about a solution that is spatially homogeneous on the membrane but inhomogeneous in the bulk [2], as well as the development of finite element [4,14–16], phase field [1], and spectral [3] numerical methods specifically adapted for bulk-membrane models. However, the behaviour of solutions to bulk-membrane coupled models beyond the onset of Turing-type instabilities has not yet been well-explored with exceptions being the study of wave-pinning phenomena using perturbation theory [4], and *in silico* exploration of the effects of domain geometry and spatial inhomogeneities for a particular model [17]. Finally, a rigorous PDE framework has recently been employed to prove well-posedness and the existence of stationary states to bulk-membrane RD models [16,18–20].

In §2–4 we outline some recent results for “far-from-equilibrium” pattern-formation phenomena in bulk-membrane coupled models. In §2 we first provide a systematic derivation of a bulk-membrane coupled model that results from the asymptotic limit of a system of coupled RD systems where one system is posed in the domain interior while the other is formulated in a thin domain that protrudes from the boundary. In §3 we highlight some results in [21] on the weakly nonlinear analysis of spatio-temporal patterns in bulk-membrane models with circular bulk geometry. In §4 we outline results from [22] for multi-spike solutions for a 1-D singularly perturbed bulk-membrane coupled Gierer-Meinhardt (GM) RD model.

A different class of RD system that involves the coupling of bulk diffusion in a multi-dimensional spatial domain to localized nonlinear processes are the bulk-cell PDE-ODE models, originating from [23] (see also [24] and [25]), and studied in a 2-D setting in [26], [27], and [28]. In these systems, a PDE bulk diffusion field, referred to as the autoinducer, mediates communication between a collection of small signalling compartments or “cells” within the domain. Intracellular nonlinear reactions, as modeled by an ODE system, can be prescribed within each cell (see Fig. 9 below). The secretion and feedback of a signaling molecule from and into the spatially localized cells allows each cell to modulate its intracellular dynamics based on the global bulk diffusion field that is produced by the entire collection of cells. This new theoretical framework is particularly relevant for modeling “cell-to-cell” bulk-mediated communication in certain microbial systems, as specific autoinducers have been experimentally identified in several such biological systems including, cAMP that triggers intracellular oscillations for a collection of

social amoebae *Dictyostelium discoideum* and acts as a precursor to guide the cells to aggregation in low nutrient environments (cf. [29], [30], [31]), and acetaldehyde (Ace) that triggers glycolytic oscillations in colonies of yeast cells (cf. [32], [33], [34]), among others.

In §5, the bulk-cell PDE-ODE model of [26] and [28] is introduced, and Sel'kov intracellular kinetics are used as a conceptual model to illustrate the sudden emergence of sustained intracellular oscillations of a collection of cells via a Hopf bifurcation, as mediated by the autoinducer field. In our model it is assumed the cells are in a quiescent state when they are uncoupled from the bulk medium. This switch-like onset of intracellular oscillations is to be contrasted with the more typical Kuramoto paradigm in which incoherently oscillating dynamically active units become increasingly synchronized as the coupling strength between the units increases (cf. [35]). For our bulk-cell PDE-ODE model, some new results for the emergence of intracellular oscillations resulting from either a single defective cell, or from a relatively large collection of non-identical cells, are given. In §6 we briefly discuss a few open problems and modeling opportunities afforded by the theoretical frameworks surveyed in §2–5.

2. Derivation of a Bulk-Membrane Coupled System

The key feature of a bulk-membrane coupled RD system is that it involves the coupling of a PDE/ODE system in an N -dimensional ($N = 2, 3$) bulk region, with a corresponding PDE/ODE system posed on its $(N - 1)$ -dimensional boundary. In the context of cell biology, such a bulk-membrane coupled model serves only as a leading order approximation under the assumption that the cell membrane is much thinner than the characteristic length scale of the cell bulk region. Here, we briefly provide a systematic derivation of such a leading order approximation.

We begin by assuming that the cell bulk region is given by a bounded domain $\Omega \subset \mathbb{R}^N$ ($N = 2, 3$) with smooth boundary $\partial\Omega$, while the cell membrane is specified by the thin domain

$$\Omega_\delta \equiv \{\mathbf{x} + \delta\eta\nu(\mathbf{x}) \mid \mathbf{x} \in \partial\Omega, 0 < \eta < 1\}, \quad (2.1)$$

where $\nu(\mathbf{x})$ is the outward unit normal at $\mathbf{x} \in \partial\Omega$ and $0 < \delta \ll 1$ is the membrane thickness. The boundary of the membrane is made up of two disjoint components corresponding to $\eta = 0$ and $\eta = 1$ in (2.1), and which we denote by $\partial\Omega_\delta^i = \partial\Omega$ and $\partial\Omega_\delta^e$, respectively.

Next, we suppose that there are $n \geq 1$ and $m \geq 1$ chemical species in the bulk and in the membrane with concentrations $U = (U_1, \dots, U_n)^T$ and $u = (\mu_1, \dots, \mu_m)^T$, respectively. In both the bulk and the membrane we assume that these chemical species undergo isotropic diffusion and reaction kinetics so that their concentrations satisfy

$$\partial_t U = D\Delta U + F(U), \quad \mathbf{x} \in \Omega; \quad D\partial_n U = q_\delta(u, U), \quad \mathbf{x} \in \partial\Omega, \quad (2.2a)$$

$$\partial_t u = d\Delta u + f_\delta(u), \quad \mathbf{x} \in \Omega_\delta; \quad d\partial_n u = -q_\delta(u, U), \quad \mathbf{x} \in \partial\Omega_\delta^i; \quad d\partial_n u = 0, \quad \mathbf{x} \in \partial\Omega_\delta^e, \quad (2.2b)$$

where ∂_n in (2.2a) and (2.2b) denotes the outward normal derivative to the boundaries of the bulk domain Ω and the thin strip Ω_δ , respectively. In (2.2), D and d are $n \times n$ and $m \times m$ diagonal matrices of bulk- and membrane-bound diffusion coefficients respectively, $F(\cdot)$ and $f_\delta(\cdot)$ denote the bulk- and membrane-bound kinetics respectively, and $q_\delta(\cdot, \cdot)$ denotes an interchange process across the bulk-membrane interface $\partial\Omega$. While we may anticipate that the bulk-bound reaction kinetics $F(\cdot)$ are independent of the membrane-thickness, the same cannot be said of the membrane-bound kinetics $f_\delta(\cdot)$ and the boundary interchange $q_\delta(\cdot, \cdot)$. Indeed, by integrating (2.2b) over Ω_δ we calculate from the divergence theorem that

$$\frac{d}{dt} \int_{\Omega_\delta} u \, d\mathbf{x} = - \int_{\partial\Omega} q_\delta(u, U) \, ds + \int_{\Omega_\delta} f_\delta(u) \, d\mathbf{x}. \quad (2.3)$$

Since $\text{vol}(\Omega_\delta) = \mathcal{O}(\delta)$ and $\text{area}(\partial\Omega) = \mathcal{O}(1)$, the three terms are balanced for $\delta \ll 1$ provided that they satisfy $\mathcal{O}(\delta)\mathcal{O}(u) = \mathcal{O}(q_\delta) = \mathcal{O}(\delta)\mathcal{O}(f_\delta)$. Enforcing that $U = \mathcal{O}(1)$, and that there is an $\mathcal{O}(1)$

exchange in (2.2a) between the bulk medium and the thin domain, (2.3) and (2.2b) imply that

$$q_\delta = \mathcal{O}(1), \quad u = \mathcal{O}(\delta^{-1}), \quad f_\delta = \mathcal{O}(\delta^{-1}). \quad (2.4)$$

To derive a leading order approximation to the bulk-membrane coupled RD system (2.2) we let $\mathbf{X}(s) \in \partial\Omega$ parametrize $\partial\Omega$, where $s = (s_1, s_2) \in \mathcal{S} \subset \mathbb{R}^2$ if $N = 3$ and $s \in \mathcal{S} \subset \mathbb{R}$ denotes the arc length along $\partial\Omega$ if $N = 2$. Next, we choose the sign of the curvature $\kappa(s)$ of $\mathbf{X}(s)$ when $N = 2$ and the orientation of the local basis (X_1, X_2) when $N = 3$ such that the unit normal

$$\nu(s) = \kappa(s)^{-1} \frac{d^2 \mathbf{X}}{ds^2} \quad (N = 2), \quad \nu(s_1, s_2) = \frac{\partial_1 \mathbf{X} \times \partial_2 \mathbf{X}}{|\partial_1 \mathbf{X} \times \partial_2 \mathbf{X}|} \quad (N = 3), \quad (2.5)$$

is outward pointing at $\mathbf{x} \in \Omega$. Each point in $\mathbf{x} \in \Omega_\delta$ is obtained in terms of the boundary fitted coordinates $(s, \eta) \in \mathcal{S} \times (0, 1)$ by $\mathbf{x} = \mathbf{X}(s) + \delta\eta\nu(s)$. The asymptotic analysis below hinges on the following expansion of the Laplacian:

$$\Delta = \begin{cases} \delta^{-2} \partial_\eta^2 + \delta^{-1} \kappa \partial_\eta - \kappa^2 \eta \partial_\eta + \Delta_{\partial\Omega} + \mathcal{O}(\delta), & N = 2, \\ \delta^{-2} \partial_\eta^2 + 2\delta^{-1} H \partial_\eta - (\kappa_1^2 + \kappa_2^2) \eta \partial_\eta + \Delta_{\partial\Omega} + \mathcal{O}(\delta), & N = 3, \end{cases} \quad (\delta \ll 1). \quad (2.6)$$

Here κ_i ($i = 1, 2$) are the principal curvatures of $\partial\Omega$, $H = (\kappa_1 + \kappa_2)/2$ is the mean curvature of $\partial\Omega$ when $N = 3$, and $\Delta_{\partial\Omega}$ is the Laplace-Beltrami operator on $\partial\Omega$. The expression (2.6) is obtained by expanding the Laplacian in terms of the curvilinear boundary-fitted coordinates (s, η) . For the remainder of this section we will denote $\Delta_{\partial\Omega} = \partial_s^2$ when $N = 2$.

Based on the scaling (2.4) we suppose that $f_\delta(u) = \delta^{-1} f(\delta u)$ and $q_\delta(u, U) = q(\delta u, U)$, and let

$$u = \delta^{-1} u_0 + u_1 + \delta u_2 + \mathcal{O}(\delta^2), \quad U = U_0 + \mathcal{O}(\delta), \quad U_0 = \mathcal{O}(1), \quad u_i = \mathcal{O}(1), \quad i = 0, 1, 2, \dots \quad (2.7)$$

We substitute this expansion into (2.2) and collect powers of δ . From the leading-order $\mathcal{O}(\delta^{-3})$ terms we get

$$d\partial_\eta u_0 = 0, \quad (s, \eta) \in \mathcal{S} \times (0, 1), \quad d\partial_\eta u_0 = 0, \quad \eta = 0, 1,$$

which implies that $u_0 = u_0(s)$. Similarly, from the $\mathcal{O}(\delta^{-2})$ problem we obtain that the first order correction is also independent of η . At next order, the $\mathcal{O}(\delta^{-1})$ problem is given by

$$\begin{aligned} \partial_t u_0 &= d\partial_\eta u_2 + d\Delta_{\partial\Omega} u_0 + f(u_0), \quad (s, \eta) \in \mathcal{S} \times (0, 1), \\ d\partial_\eta u_2 &= q(u_0, U_0), \quad \eta = 0, \quad d\partial_\eta u_2 = 0, \quad \eta = 1. \end{aligned}$$

Upon integrating the PDE for u_0 over $0 < \eta < 1$, and using the two boundary conditions for u_2 and the η -independence of u_0 , we obtain that (2.2) is, to leading order in $\delta \ll 1$, approximated by

$$\partial_t U_0 = D\Delta U_0 + F(U_0), \quad \mathbf{x} \in \Omega, \quad D\partial_n U_0 = q(u_0, U_0), \quad \mathbf{x} \in \partial\Omega, \quad (2.8a)$$

$$\partial_t u_0 = d\Delta_{\partial\Omega} u_0 + f(u_0) - q(u_0, U_0), \quad \mathbf{x} \in \partial\Omega. \quad (2.8b)$$

3. Weakly Nonlinear Patterns in Bulk-Membrane Systems

Here we highlight the multiple-scale expansion approach of [21] for the derivation of amplitude, or normal form, equations for a variety of spatio-temporal patterns in a class of coupled bulk-membrane RD models with circular bulk geometry. Moreover, we discuss some results obtained from these normal forms, and we illustrate some new ‘‘far-from-equilibrium’’ patterns that are observed. In the formulation, we assume that two bulk species U, V undergo passive diffusion but with a linear decay of their bulk kinetics in a 2-D disk domain of radius R . In terms of polar coordinates r and θ , the bulk species are assumed to satisfy

$$U_t = D_u \left(U_{rr} + r^{-1} U_r + r^{-2} U_{\theta\theta} \right) - \sigma_u U, \quad V_t = D_v \left(V_{rr} + r^{-1} V_r + r^{-2} V_{\theta\theta} \right) - \sigma_v V, \quad (3.1)$$

in $0 < r < R$ and $0 \leq \theta < 2\pi$. Here D_u, D_v and σ_u, σ_v are positive constants indicating the diffusion and degradation coefficients for each species. Next, we use Robin-type boundary

conditions to model the exchange near the boundary between the bulk species and the membrane-bound species, denoted as u , v , as

$$D_u U_r = \alpha(u, U), \quad D_v V_r = \beta(v, V), \quad r = R, \quad (3.2)$$

with arbitrary flux terms $\alpha(u, U)$ and $\beta(v, V)$. Finally, the dynamics of the membrane-bound species is assumed to be governed by the following nonlinear RD system:

$$u_t = \frac{d}{R^2} u_{\theta\theta} - \alpha(u, U) + f(u, v), \quad v_t = \frac{d}{R^2} v_{\theta\theta} - \beta(v, V) + g(u, v), \quad r = R, \quad (3.3)$$

where $d > 0$ is the surface diffusion coefficient, assumed to be a common constant to both u and v , while $f(u, v)$ and $g(u, v)$ are arbitrary nonlinear kinetics. Our aim here by assuming the same rate of lateral diffusion is to avoid the short-range activation and long-range inhibition paradigm, as has been typical for the conventional study of diffusion-driven instabilities. As a result, the spatio-temporal patterns illustrated below directly results from the bulk-membrane coupling.

In §3.1, we outline how to derive amplitude equations characterizing the branching behaviour and local stability of spatio-temporal patterns near Hopf and pitchfork bifurcation points. Three numerical examples illustrating the weakly nonlinear theory are given. In §3.2 we explore the formation of large amplitude rotating waves that occur in the nonlinear regime away from $O(2)$ symmetric Hopf bifurcation points. The full numerical results shown below are obtained via numerical continuation of a finite element discretization of the coupled bulk-membrane model (3.1)–(3.3) as implemented by the Matlab bifurcation package *pde2path* (cf. [36,37]).

3.1 Weakly Nonlinear Analysis: Amplitude Equations

Multi-scale expansion methods have been widely used to derive amplitude equations characterizing the onset of spatio-temporal patterns in various PDE systems (cf. [38,39]). We now show how it can be extended to the coupled bulk-membrane model defined by (3.1)–(3.3). To illustrate the weakly nonlinear theory, we assume that $\alpha(u, U)$ and $\beta(v, V)$ in (3.2) are linear of the form

$$\alpha(u, U) = K_u(u - U), \quad \beta(v, V) = K_v(v - V), \quad (3.4)$$

where K_u, K_v are two constant coupling parameters. In addition, we will use prototypical Brusselator reaction kinetics for the two nonlinearities $f(u, v)$ and $g(u, v)$ in (3.3), given by

$$f(u, v) = a - (b + 1)u + u^2 v, \quad g(u, v) = bu - u^2 v. \quad (3.5)$$

Here we assume that $b < a^2 + 1$, so that for the uncoupled case ($K_u = K_v = 0$) there exists a unique spatially uniform steady state to (3.3) that is linearly stable. First, it is convenient to rewrite the coupled bulk-membrane model as a nonlinear evolution equation in the form

$$\dot{W} = \mathbf{F}(W; \mu) = \begin{pmatrix} D_u \Delta U - \sigma_u U \\ D_v \Delta V - \sigma_v V \\ \frac{d}{R^2} u_{\theta\theta} - K_u(u - U)|_{r=R} + f(u, v) \\ \frac{d}{R^2} v_{\theta\theta} - K_v(v - V)|_{r=R} + g(u, v) \end{pmatrix}, \quad (3.6)$$

where $\mu \in \mathbb{R}^p$ is some vector of bifurcation parameters, and where $W \equiv (U, V, u, v)^T$ satisfies

$$D_u \frac{\partial U}{\partial r} = K_u(u - U), \quad D_v \frac{\partial V}{\partial r} = K_v(v - V), \quad r = R. \quad (3.7)$$

We readily calculate that a radially symmetric steady state solution to (3.6) is given by

$$W_e(r) = \begin{pmatrix} \frac{K_u u_e I_0(\omega_u r)}{D_u \omega_u I_1(\omega_u R) + K_u I_0(\omega_u R)} \\ \frac{K_v v_e I_0(\omega_v r)}{D_v \omega_v I_1(\omega_v R) + K_v I_0(\omega_v R)} \\ u_e \\ v_e \end{pmatrix}, \quad \omega_u \equiv \sqrt{\frac{\sigma_u}{D_u}}, \quad \omega_v \equiv \sqrt{\frac{\sigma_v}{D_v}}, \quad (3.8)$$

where $I_n(z)$ is the usual modified Bessel function. Here the membrane-bound, spatially uniform, steady state vector $(u_e, v_e)^T$ is a solution of the nonlinear algebraic problem

$$\frac{K_u}{1 + \frac{K_u}{\sqrt{D_u \sigma_u}} \frac{I_0(\omega_u R)}{I_1(\omega_u R)}} u_e - f(u_e, v_e) = 0, \quad \frac{K_v}{1 + \frac{K_v}{\sqrt{D_v \sigma_v}} \frac{I_0(\omega_v R)}{I_1(\omega_v R)}} v_e - g(u_e, v_e) = 0. \quad (3.9)$$

To analyze the linear stability of this base state, we introduce the perturbation

$$W(r, \theta, t) = W_e(r) + \mathcal{W}_n(r) e^{in\theta + \lambda t}, \quad (3.10)$$

where $\lambda \in \mathbb{C}$ is the growth rate of the perturbation and $n \in \mathbb{Z}$ is its spatial wave number. By solving the linearized problem, we readily obtain in terms of modified Bessel functions that

$$\mathcal{W}_n(r) = \begin{pmatrix} \frac{K_u u_n I_n(\Omega_u r)}{D_u \Omega_u I_n'(\Omega_u R) + K_u I_n(\Omega_u R)} \\ \frac{K_v v_n I_n(\Omega_v r)}{D_v \Omega_v I_n'(\Omega_v R) + K_v I_n(\Omega_v R)} \\ u_n \\ v_n \end{pmatrix}, \quad \Omega_u \equiv \sqrt{\frac{\lambda + \sigma_u}{D_u}}, \quad \Omega_v \equiv \sqrt{\frac{\lambda + \sigma_v}{D_v}}. \quad (3.11)$$

Here the eigenvector $(u_n, v_n)^T$ is a nontrivial solution of the 2×2 homogeneous matrix problem

$$\begin{pmatrix} \lambda + \frac{n^2 d}{R^2} + \frac{K_u}{1 + \frac{K_u}{D_u \Omega_u} \frac{I_n(\Omega_u R)}{I_n'(\Omega_u R)}} - \frac{\partial f}{\partial u} & -\frac{\partial f}{\partial v} \\ -\frac{\partial g}{\partial u} & \lambda + \frac{n^2 d}{R^2} + \frac{K_v}{1 + \frac{K_v}{D_v \Omega_v} \frac{I_n(\Omega_v R)}{I_n'(\Omega_v R)}} - \frac{\partial g}{\partial v} \end{pmatrix} \begin{pmatrix} u_n \\ v_n \end{pmatrix} = \begin{pmatrix} 0 \\ 0 \end{pmatrix}, \quad (3.12)$$

which occurs for those values of λ (eigenvalues) for which the determinant of the matrix in (3.12) vanishes. In (3.12) all partial derivatives are evaluated at the radially symmetric steady state.

To illustrate the weakly nonlinear theory we will only consider pitchfork bifurcations for $n \neq 0$ and Hopf bifurcations that are associated with the trivial wave number $n = 0$ as the coupling rate K_v and the bulk diffusivity D_v are simultaneously varied. The intricate case of codimension-two pitchfork-Hopf bifurcations, near which oscillating spatial patterns occur, is also treated in [21]. The effect of Hopf instabilities associated with modes $n \neq 0$ are discussed in §3.2.

The key idea of a multi-scale analysis is to use the distance from some bifurcation point as a small parameter $\sigma \ll 1$ to define a slow time-scale $\tau = \sigma^2 t$. Hence, we let $\mu = (K_v, D_v)^T$ be a bifurcation parameter vector and we expand it near a bifurcation point μ_0 as

$$\mu \equiv (K_v, D_v)^T = \mu_0 + \sigma^2 \mu_1, \quad \|\mu_1\| \equiv 1, \quad (3.13)$$

where $\mu_1 \in \mathbb{R}^2$ is a detuning parameter indicating the direction of the bifurcation in parameter space. By choosing the bifurcation parameter μ as a two-vector, the bifurcation behavior of solutions along various slices through the (K_v, D_v) phase diagram is more readily analyzed (cf. [21]).

Next, we denote $W \equiv W(r, \theta, t, \tau)$ and introduce the following regular asymptotic expansion:

$$W = W_e + \sigma W_1 + \sigma^2 W_2 + \sigma^3 W_3 + \mathcal{O}(\sigma^4). \quad (3.14)$$

Upon substituting (3.14) in (3.6) and (3.7), we obtain a series of linear systems to be solved at each order $\mathcal{O}(\sigma^j)$. At $\mathcal{O}(1)$, we have the steady state problem $\mathbf{F}(W_e; \mu_0) = 0$, which is automatically satisfied. Next, there are two possible solutions to the $\mathcal{O}(\sigma)$ problem, which corresponds to the linearized system, depending on the specific bifurcation considered. If the system undergoes a Hopf bifurcation at μ_0 with critical eigenvalues $\lambda = \pm i\lambda_I$, we write

$$W_1 = A_0(\tau) \mathcal{W}_0 e^{i\lambda_I \tau} + \overline{A_0(\tau)} \overline{\mathcal{W}_0} e^{-i\lambda_I \tau}, \quad (3.15)$$

while for the steady case of a pitchfork bifurcation we introduce the following ansatz:

$$W_1 = \mathcal{W}_n \left[A_n(\tau) e^{in\theta} + \overline{A_n(\tau)} e^{-in\theta} \right], \quad n \neq 0. \quad (3.16)$$

The amplitude coefficients $A_n(\tau)$ in (3.15) and (3.16) are at this stage unknown, but evolution equations governing their dynamics on the slow time-scale are readily derived upon applying a

solvability condition on the inhomogeneous linear system defined by the $\mathcal{O}(\sigma^3)$ problem (see §2 of [21]). In this way, the amplitude or normal form ODE for the case of a Hopf bifurcation is given by

$$\frac{dA_0}{d\tau} = g_{1000}^T \mu_1 A_0 + g_{2100} |A_0|^2 A_0, \quad (3.17)$$

with complex coefficients $g_{1000} \in \mathbb{C}^2$ and $g_{2100} \in \mathbb{C}$, where $\mu_1 \in \mathbb{R}^2$ measures the deviation of the bifurcation point from criticality (see (3.13)). Similarly, for a pitchfork bifurcation we obtain

$$\frac{dA_n}{d\tau} = g_{0010}^T \mu_1 A_n + g_{0021} |A_n|^2 A_n, \quad n \neq 0, \quad (3.18)$$

where both coefficients $g_{0010} \in \mathbb{R}^2$ and $g_{0021} \in \mathbb{R}$ are real. The normal form ODEs (3.17) and (3.18), also known as Stuart-Landau equations, are special cases of the Ginzburg-Landau equations with no diffusion terms, and have the same form as amplitude equations derived for a weakly nonlinear analysis of patterns in RD systems on bounded domains. Explicit formulae for g_{1000} , g_{2100} , g_{0010} and g_{0021} , for the coupled bulk-membrane problem, are derived in [21].

The steady states of (3.17) and (3.18) have a clear interpretation in terms of spatio-temporal patterns of the coupled bulk-membrane model. For instance, (3.18) admits a trivial steady state $A_n = 0$, corresponding to the radially symmetric steady state. When it exists, the nontrivial steady-state A_{ne} of (3.18) satisfies

$$|A_{ne}| = \sqrt{-\frac{g_{0010}^T \mu_1}{g_{0021}}}, \quad (3.19)$$

and is stable if and only if the cubic term coefficient g_{0021} is negative. In this case, the pitchfork bifurcation is supercritical and a stable steady state pattern is expected near the bifurcation point μ_0 . Alternatively, if $g_{0021} > 0$, the pitchfork bifurcation is said to be subcritical and the pattern is unstable. Finally, we readily obtain the following asymptotic approximation for a family of steady state patterns in the weakly nonlinear regime:

$$W = W_e + \sigma A_{ne} \mathcal{W}_n \left[e^{i(n\theta + \phi)} + e^{-i(n\theta + \phi)} \right] + \mathcal{O}(\sigma^2), \quad (3.20)$$

where $\phi \in \mathbb{R}$ is an arbitrary phase shift added owing to the $O(2)$ equivariance. A similar analysis applies to (3.17), with the difference being that the coefficients are complex-valued (see §3 of [21]).

To illustrate our weakly nonlinear results, we first show in Fig. 1 how the transition between supercritical and subcritical Hopf bifurcations can be captured simply by numerically evaluating $\Re(g_{2100})$ along a stability boundary in the D_v versus K_v parameter plane. Weakly nonlinear analyses can sometimes detect very delicate phenomena, which would not easily be captured just from a time-dependent numerical simulation. This is the case for the global bifurcation diagram shown in the middle panel, where the family of periodic solutions is stable only in a very small window near the supercritical Hopf bifurcation. However, away from the Hopf bifurcation point both branches possess a fold point connecting unstable limit cycles to stable radially symmetric relaxation-type oscillations. Finally, as $\sigma = \sqrt{\|\mu - \mu_0\|} \rightarrow 0$, the asymptotic approximations of spatio-temporal patterns become increasingly accurate. This is illustrated in the middle panels of Fig. 2 and 3, where one can observe a very good agreement between the full PDE numerics and the weakly nonlinear prediction (3.20) near a subcritical and a supercritical pitchfork bifurcation, respectively. Upon comparing the corresponding global bifurcation diagrams shown in the left panels of Fig. 2 and 3, we observe that the weakly nonlinear theory for the subcritical case does not agree as well with the full numerics away from the bifurcation point as it does for the supercritical case. This is likely due to the existence of a nearby saddle-node (secondary) bifurcation point on the global bifurcation diagram for the case of a subcritical pitchfork bifurcation.

3.2 Far from Equilibrium Dynamics: Formation of Rotating Waves

A Hopf bifurcation in the presence of $O(2)$ symmetry (for instance resulting from periodic boundary conditions) generically leads to the formation of standing and rotating waves (cf. [40]).

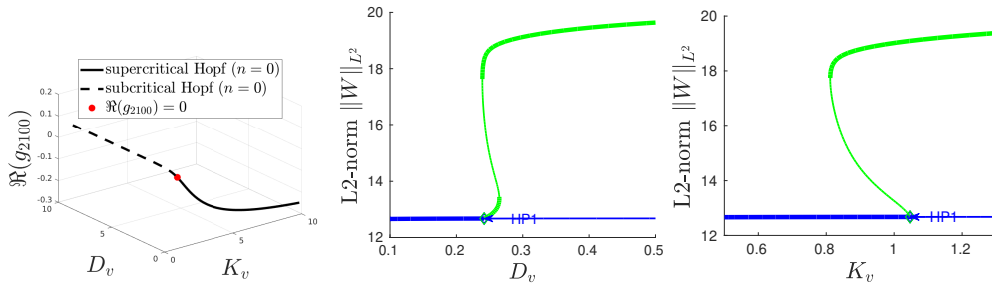


Figure 1: Left: Hopf stability boundaries in the D_v vs. K_v parameter plane. The vertical axis is the real part of the cubic term coefficient in (3.17). The red dot is the transition point between the sub- and supercritical regimes. Middle: Supercritical Hopf bifurcation on the slice $K_v = 10$. Right: Subcritical Hopf bifurcation on the slice $D_v = 10$. Stable branches in these panels are indicated by heavy curves. Parameters: $R = 1$, $D_u = 1$, $\sigma_u = \sigma_v = 0.01$, $K_u = 0.1$, $d = 0.5$, $a = 3$, and $b = 8.7$. The Hopf bifurcation points are labelled by HP1.

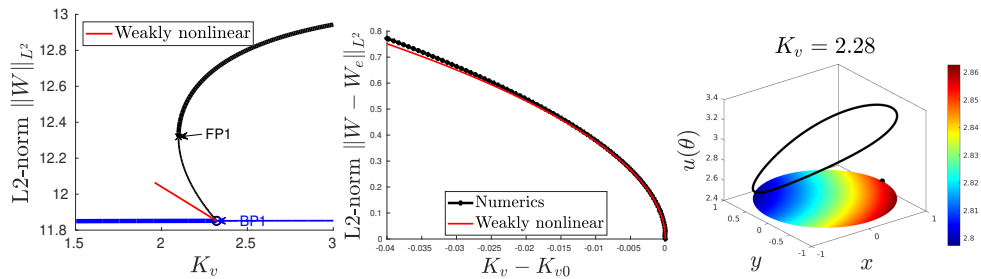


Figure 2: Left: Subcritical pitchfork bifurcation as a function of K_v , with stable branches indicated by heavy curves. The red curve is the asymptotic prediction (3.20). Middle: The numerical and weakly nonlinear solutions agree well after subtracting with the trivial branch and shifting the bifurcation point to the origin. Right: A numerically computed unstable pattern for the bulk density $U(r, \theta)$ and the membrane-bound species $u(\theta)$ near the subcritical pitchfork bifurcation. Parameters: $R = 1$, $D_u = 1$, $D_v = 10$, $\sigma_u = \sigma_v = 0.01$, $K_u = 0.1$, $d = 0.5$, $a = 3$, and $b = 7.5$. In the left panel, BP1 and FP1 indicate the pitchfork and saddle-node (secondary) bifurcation points, respectively. The black dot in the right panel is the point $\mathbf{x} = (1, 0)^T$, where $\theta = 0$, on the boundary of the unit disk.

In §5 of [21], the formation of left and right rotating waves around a circular bulk domain was briefly numerically explored for a special case of the model (3.1)–(3.3) with coupling functions

$$\alpha(u, U) = r_d u - r_a U, \quad \beta(v, V) = p_d v - p_a V, \quad (3.21)$$

and Brusselator reaction kinetics (3.5) on the boundary. In Fig. 4 we provide a new result for the global bifurcation diagram, as obtained with *pde2path*, where branches of rotating waves are computed as relative equilibria in a moving frame with speed $s = 2\pi R/(nT)$, where n is the wave number and T is the period (see [41] for details of the algorithm). In this figure, the stable $n = 0$ branch (green curve) corresponds to a family of radially symmetric periodic solutions and is easily computed as periodic orbits in a static frame. As the reaction rate b increases in (3.5), we remark that the $n = 1$ rotating wave branch (black curve) gains stability in a Hopf bifurcation near $b \approx 7.04$, where an unstable branch of modulated waves emerge (cyan curve). This critical value is labelled by the black HP₁ point in Fig. 4. The $n = 2$ rotating wave branch (red curve), originating at HP₃ in Fig. 4, is unstable for the parameter regime considered. A few snapshots of the stable $n = 1$ rotating wave are presented in Fig. 5. We also suspect the presence of unstable branches of standing waves near the $n = 1$ and $n = 2$ rotating wave branches, but these branches were not computed.

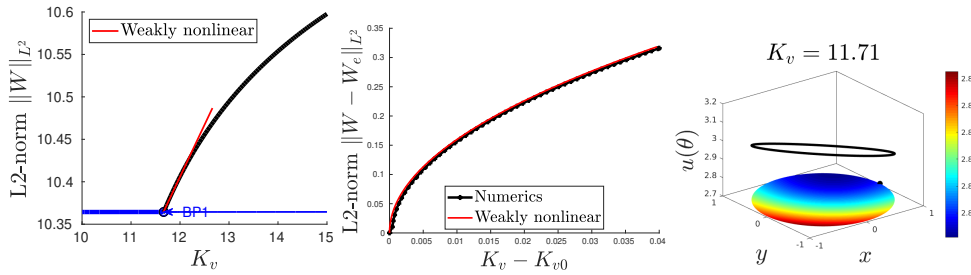


Figure 3: Left: Supercritical pitchfork bifurcation as a function of K_v , with stable branches indicated by heavy curves. The red curve is the asymptotic prediction (3.20). Middle: The numerical and weakly nonlinear solutions agree well after subtracting with the trivial branch and shifting the bifurcation point to the origin. Right: A numerically computed stable pattern for the bulk density $U(r, \theta)$ and the membrane-bound species $u(\theta)$ near the supercritical pitchfork bifurcation. Parameters: $d = 1$ and $b = 5$, and with others as in Fig. 2. BP1 is the pitchfork bifurcation point and the black dot in the right panel is the point $\mathbf{x} = (1, 0)^T$, where $\theta = 0$.

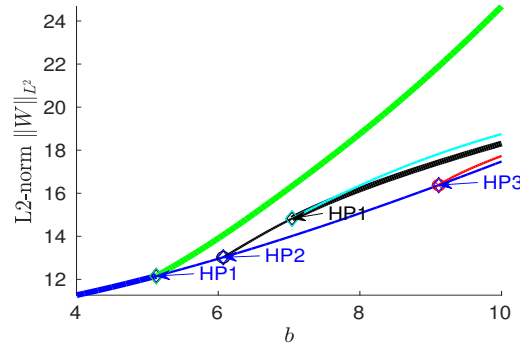


Figure 4: Branch of periodic orbits emerging from Hopf bifurcations associated with wave numbers $n = 0$ (green), $n = 1$ (black) and $n = 2$ (red), as a function of the reaction rate b in the Brusselator kinetics (3.5) and with the Robin coupling (3.21). The cyan curve (near the $n = 1$ branch of rotating waves) corresponds to the unstable branch of modulated waves. Stable branches are indicated by heavy lines. Parameters: $R = 1$, $D_u = D_v = 1$, $\sigma_u = \sigma_v = 0.5$, $d = 0.5$, $r_a = 0.1$, $r_d = 1$, $p_a = 1$, $p_d = 0.1$, and $a = 3$. The first, second, and third Hopf bifurcation points on the steady-state branch (blue curve) are labelled by HP₁, HP₂, and HP₃ respectively. The Hopf bifurcation point on the $n = 1$ branch where stability is re-gained is indicated by the black HP₁ point, which occurs for $b \approx 7.4$.

4. Spike Solutions in a Bulk-Membrane Coupled GM Model

The GM model [42] is a prototypical activator-inhibitor RD system that, in the limit of an asymptotically small activator diffusivity, has been well-studied using both rigorous and asymptotic techniques [43–46]. By assuming that the inhibitor shuttles between a membrane- and bulk-bound state, while the activator is solely membrane-bound, the authors of [22] extended the previous asymptotic theory by incorporating bulk-membrane coupling. In this section we highlight some results of [22] for a bulk-membrane coupled GM model, especially as they pertain to the effects of bulk-membrane coupling on the existence and linear stability of symmetric multi-spike solutions. Specifically, for a bounded 2-D domain Ω with a smooth boundary $\partial\Omega$ of perimeter $L > 0$, we consider the membrane-bound GM model

$$\partial_t u = \varepsilon^2 \partial_\sigma^2 u - u + u^3/v, \quad 0 < \sigma < L, \quad t > 0, \quad (4.1a)$$

$$\tau_s \partial_t v = D_v \partial_\sigma^2 v - (1 + K)v + KV + \varepsilon^{-1} u^3, \quad 0 < \sigma < L, \quad t > 0, \quad (4.1b)$$

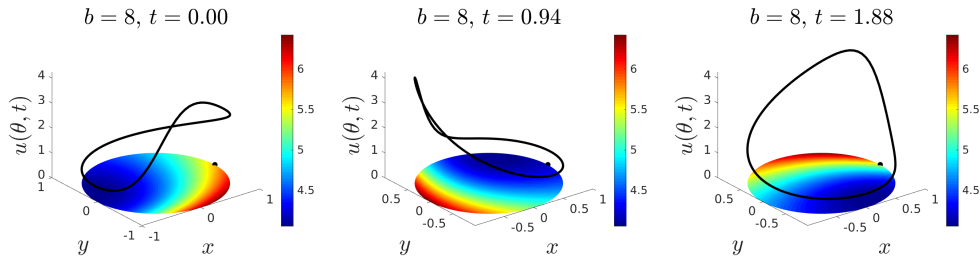


Figure 5: Snapshots of a numerically computed stable rotating wave with $b = 8$ and wave number $n = 1$, corresponding to a point on the heavy solid black curve in Fig. 4. Each frame corresponds to $1/3$ of the period $T \approx 2.82$, and the speed is $s = 2\pi/T \approx 2.23$. Other parameters as in Fig. 4. The black dot corresponds to the point $\mathbf{x} = (1, 0)^T$ where $\theta = 0$.

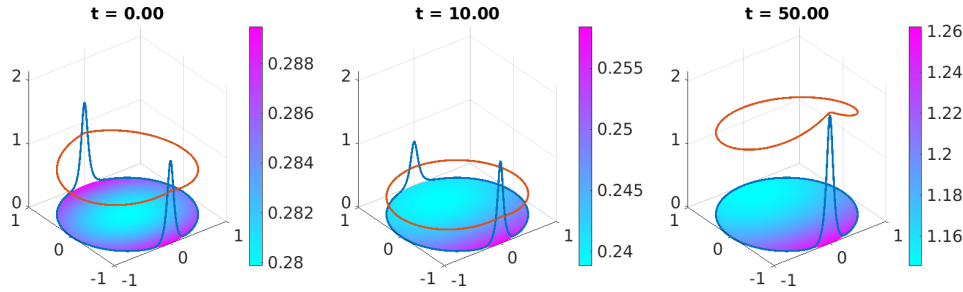


Figure 6: A symmetric two-spike steady state pattern undergoes a competition instability leading to a spike collapse event. Result shows the membrane-bound activator (blue) and inhibitor (orange) values as well as the bulk-bound inhibitor (colourmap) values, as obtained from a PDE numerical simulation of the bulk-membrane coupled GM model (4.1) with $\varepsilon = 0.05$, $D_b = 10$, $D_v = 10$, $\tau_s = 0.6$, $\tau_b = 0.1$, and $K = 2$.

where σ denotes the arc-length along the boundary, and u and v are the concentrations of the membrane-bound activator and inhibitor, respectively. The activator diffusivity ε^2 is assumed to be asymptotically small, while the remaining parameters are taken as $\mathcal{O}(1)$ with respect to $\varepsilon \ll 1$. The inhibitor field v for this membrane-bound problem is coupled to the bulk solution V , the latter of which satisfies the linear diffusion equation

$$\tau_b \partial_t V = D_b \Delta V - V, \quad \mathbf{x} \in \Omega, \quad D_b \partial_n V + KV = Kv, \quad \mathbf{x} \in \partial\Omega. \quad (4.1c)$$

Here τ_b and D_b , as well as the coupling parameter $K \geq 0$, are $\mathcal{O}(1)$ with respect to $\varepsilon \ll 1$. In §4.1 we outline the asymptotic analysis for the construction of multi-spike equilibria for this bulk-coupled model (4.1). In §4.2 we outline the linear stability analysis of symmetric multi-spike equilibria.

We remark that our particular choice of GM exponents in (4.1) yields an *explicitly solvable* nonlocal eigenvalue problem (NLEP) that considerably simplifies the stability analysis (see equation (4.10) below), but that retains qualitatively similar phenomena as that which occurs with the prototypical GM exponent set and for other more general GM exponent sets (see [22]). Particular choices of the exponent sets for the nonlinearities in the generalized GM model for which the spectrum of the associated NLEP can be reduced more tractably to the study of certain explicit transcendental equations in the eigenvalue parameter were first identified in [47]. These nonlocal spectral problems were referred to in [47] as *explicitly solvable NLEPs*.

4.1 Multi-Spike Equilibrium Solutions

The key feature of (4.1) that allows for a detailed asymptotic construction and analysis of its equilibrium solutions is the asymptotically small diffusivity of the activator. Indeed, for $\varepsilon \rightarrow 0$, steady states for the activator field consist of several $\mathcal{O}(1)$ peaks, or “spikes”, that are concentrated in a disjoint finite collection of $\mathcal{O}(\varepsilon)$ intervals. Such *strongly localized* solutions, characterized by large amplitude perturbations confined to asymptotically small regions, are commonly found in a wide class of singularly perturbed linear and non-linear problems (see [48] for an overview).

By using the method of matched asymptotic expansions, the problem of constructing a multi-spike equilibrium solution to (4.1) can be reduced to a finite-dimensional problem of determining the location and height of each spike. Specifically, in the limit $\varepsilon \rightarrow 0^+$, an N -spike pattern with spikes concentrating at $0 \leq \sigma_1, \dots, \sigma_N < L$ is given asymptotically by (see Proposition 2.1 of [22])

$$u_e(\sigma) \sim \sum_{j=1}^N v_{ej}^{1/2} w(\varepsilon^{-1}[\sigma - \sigma_j]), \quad v_e(\sigma) \sim \sqrt{2\pi} \sum_{j=1}^N v_{ej}^{3/2} G_{\partial\Omega}^0(\sigma, \sigma_j), \quad (4.2a)$$

$$V_e(\mathbf{x}) \sim \sqrt{2\pi} K \sum_{j=1}^N v_{ej}^{3/2} \int_0^L G_{\Omega}^0(\mathbf{x}, \tilde{\sigma}) G_{\partial\Omega}^0(\tilde{\sigma}, \sigma_j) d\tilde{\sigma}, \quad (4.2b)$$

where v_{e1}, \dots, v_{eN} are the undetermined spike heights. In (4.2), $G_{\Omega}^0(\mathbf{x}, \tilde{\sigma})$ is the bulk Robin Green’s function satisfying (with $\lambda = 0$)

$$D_b \Delta_{\mathbf{x}} G_{\Omega}^{\lambda}(\mathbf{x}, \tilde{\sigma}) - \mu_{b\lambda}^2 G_{\Omega}^{\lambda}(\mathbf{x}, \tilde{\sigma}) = 0, \quad \mathbf{x} \in \Omega, \quad (4.3a)$$

$$D_b \partial_n G_{\Omega}^{\lambda}(\mathbf{x}(\sigma), \tilde{\sigma}) + K G_{\Omega}^{\lambda}(\mathbf{x}(\sigma), \tilde{\sigma}) = \delta(\sigma - \tilde{\sigma}), \quad \mathbf{x}(\sigma) \in \partial\Omega, \quad (4.3b)$$

where $\mu_{b\lambda} \equiv \sqrt{1 + \tau_b \lambda}$, while $G_{\partial\Omega}^0$ is the nonlocal membrane-bound Green’s function satisfying

$$D_v \partial_{\sigma}^2 G_{\partial\Omega}^{\lambda}(\sigma, \zeta) - \mu_{s\lambda}^2 G_{\partial\Omega}^{\lambda}(\sigma, \zeta) + K^2 \int_0^L G_{\Omega}^{\lambda}(\mathbf{x}(\sigma), \tilde{\sigma}) G_{\partial\Omega}^{\lambda}(\tilde{\sigma}, \zeta) d\tilde{\sigma} = -\delta(\sigma - \zeta), \quad (4.4)$$

where $0 < \sigma, \zeta < L$ and $\mu_{s\lambda} \equiv \sqrt{1 + K + \tau_s \lambda}$. The function $w(y) = \sqrt{2} \operatorname{sech} y$ is the homoclinic solution of $w'' - w + w^3 = 0$ with $w'(0) = 0$, $w(0) > 0$, and $w \rightarrow 0$ as $|y| \rightarrow \infty$. By matching *inner* and *outer* asymptotic expansions, and upon deriving a higher-order solvability condition, it was shown in §2.1 of [22] that the spike heights and locations satisfy the nonlinear algebraic system

$$v_{ei} = \sqrt{2\pi} \sum_{j=1}^N v_{ej}^{3/2} G_{\partial\Omega}^0(\sigma_i, \sigma_j), \quad v_{ei}^{3/2} \langle \partial_{\sigma} G_{\partial\Omega}^0(\sigma, \sigma_i) \rangle_{\sigma_i} + \sum_{j \neq i}^N v_{ej}^{3/2} \partial_{\sigma} G_{\partial\Omega}^0(\sigma_i, \sigma_j) = 0, \quad (4.5)$$

for $i = 1, \dots, N$, where we have defined $\langle f \rangle_{\sigma_i} \equiv \frac{1}{2} \lim_{h \rightarrow 0^+} [f(\sigma_i + h) + f(\sigma_i - h)]$. When Ω is the unit disk or when $D_b \rightarrow \infty$ we can calculate G_{Ω}^0 and $G_{\partial\Omega}^0$ explicitly. In this way, from (4.5) the spike locations and heights of a *symmetric* N -spike equilibrium solution are given by

$$\sigma_i = (i - 1)L/N, \quad v_{ei} = v_{e0} \equiv \left[\sqrt{2\pi} \sum_{k=0}^{\infty} G_{\partial\Omega}^0\left(\frac{kL}{N}, 0\right) \right]^{-2}, \quad i = 1, \dots, N. \quad (4.6)$$

The left panel of Fig. 6 shows a steady state two-spike pattern on the boundary of the unit disk.

4.2 Linear Stability of Symmetric N -Spike Equilibria

The linear stability properties of the symmetric N -spike equilibrium pattern, as given asymptotically by (4.2) and (4.6), is obtained by introducing the perturbation $u(\sigma) = u_e(\sigma) + e^{\lambda t} \phi(\sigma)$, $v(\sigma) = v_e(\sigma) + e^{\lambda t} \psi(\sigma)$, and $V(\mathbf{x}) = V_e(\mathbf{x}) + e^{\lambda t} \eta(\mathbf{x})$ into (4.1) and linearizing the

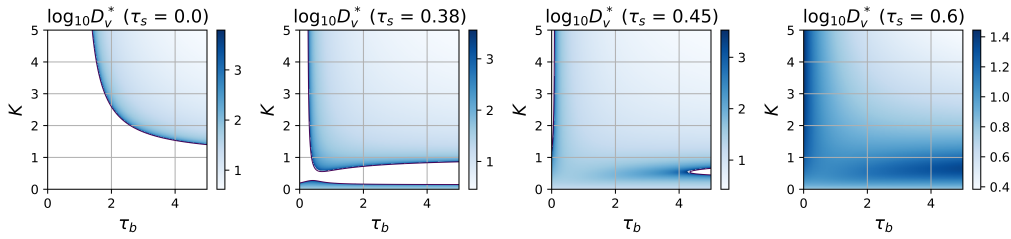


Figure 7: Colourmap of the ($k=0$) Hopf instability threshold D_v^* in the (K, τ_b) parameter plane when $D_b \rightarrow \infty$ for select values of $\tau_s \geq 0$ with $L = 2\pi$ and $A = \pi$. The unshaded regions correspond to those parameter values for which synchronous instabilities do not exist.

resulting system. This yields the singularly perturbed eigenvalue problem

$$\varepsilon^2 \partial_\sigma^2 \phi - \phi + 3u_e^2 v_e^{-1} \phi - u_e^3 v_e^{-2} \psi = \lambda \phi, \quad 0 < \sigma < L, \quad (4.7a)$$

$$D_v \partial_\sigma^2 \psi - \mu_s^2 \lambda \psi + K \eta = -3\varepsilon^{-1} u_e^2 \phi, \quad 0 < \sigma < L, \quad (4.7b)$$

$$D_b \Delta \eta - \mu_b^2 \lambda \eta = 0, \quad \mathbf{x} \in \Omega; \quad D_b \partial_n \eta + K \eta = K \psi, \quad \mathbf{x} \in \partial\Omega. \quad (4.7c)$$

It can be shown that this spectral problem admits both *large* and *small* eigenvalues for which $\lambda = \mathcal{O}(1)$ and $\lambda = \mathcal{O}(\varepsilon^2)$, respectively. The small eigenvalues are related to the stability of the N -spike pattern with respect to slow drift dynamics and are expected to be stable due to the symmetry properties of the symmetric N -spike steady-state. On the other hand, the stability properties with respect to the large eigenvalues can be determined by first using the method of matched asymptotic expansions to reduce (4.7) to a system of NLEPs, which can be analyzed.

To determine the stability with respect to the large eigenvalues of (4.7) we first let $\mathcal{G}_{\partial\Omega}^\lambda$ denote the symmetric $N \times N$ matrix with entries $(\mathcal{G}_{\partial\Omega}^\lambda)_{ij} = G_{\partial\Omega}^\lambda(\sigma_i, \sigma_j)$ for $i, j = 1, \dots, N$. Since $\mathcal{G}_{\partial\Omega}^\lambda$ is also circulant, its eigenvalues $\mu_k(\lambda)$ and corresponding eigenvectors \mathbf{c}_k are given explicitly by

$$\mu_k(\lambda) = \sum_{j=0}^{N-1} G_{\partial\Omega}^\lambda(jL/N, 0) e^{i \frac{2\pi j k}{N}}, \quad \mathbf{c}_k = (1, e^{i \frac{2\pi k}{N}}, \dots, e^{i \frac{2\pi(N-1)k}{N}})^T, \quad (4.8)$$

for $k = 0, \dots, N-1$. By using the method of matched asymptotic expansions it was shown in [22] that an eigenfunction of (4.7) has the form $\phi(\sigma) \sim \sum_{j=1}^N c_{kj} \Phi_k(\varepsilon^{-1}[\sigma - \sigma_j])$ where c_{kj} is the j^{th} entry of \mathbf{c}_k . Here, for each mode k , λ is an eigenvalue of an NLEP for $\Phi_k(y)$ given by

$$\Phi_k'' - \Phi_k + 3w^2 \Phi_k - \frac{3\mu_k(\lambda)}{\mu_k(0)} w^3 \frac{\int_{-\infty}^{\infty} w^2 \Phi_k dy}{\int_{-\infty}^{\infty} w^3 dy} = \lambda \Phi_k, \quad k = 0, \dots, N-1, \quad (4.9)$$

which is posed on $-\infty < y < \infty$ with $\Phi_k \rightarrow 0$ as $y \rightarrow \pm\infty$. Due to our specific choice of GM exponents, it was shown in [22] (see also [47]) that (4.9) is explicitly solvable in the sense that any discrete eigenvalue λ of the NLEP must be a root of the transcendental equation

$$\frac{\mu_0(0)}{\mu_k(\lambda)} - \frac{9}{2(3-\lambda)} = 0, \quad k = 0, \dots, N-1. \quad (4.10)$$

The N -spike steady-state is linearly stable if the union of all the roots λ to (4.10) satisfy $\Re(\lambda) < 0$.

Since $\mathbf{c}_0 = (1, \dots, 1)^T$ whereas $\mathbf{c}_0^T \mathbf{c}_k = 0$ for all $1 \leq k \leq N-1$ we conclude that unstable spectra for these modes correspond to either synchronous or asynchronous instabilities of the spike amplitudes, respectively. For synchronous instabilities the spikes have a common amplitude perturbation, in contrast to asynchronous instabilities where the sum of the perturbations of the spike amplitudes is zero. This latter type of instability is also referred to as a competition instability since the amplitude of some of the spikes increases at the expense of a decrease in the amplitude of other spikes (cf. [22]). In [22] it is found that the synchronous instabilities occur

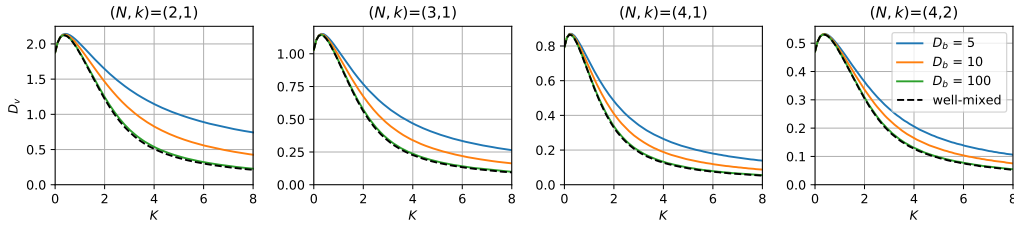


Figure 8: Competition instability threshold D_v versus coupling parameter $K \geq 0$ for different number of spikes $N = 2, 3, 4$ and asynchronous instability modes k . The legend in the right-most plot applies to each plot. This threshold is independent of τ_s and τ_b . The left-most plot shows that a two-spike steady-state is unstable for the parameters in Fig. 6 where $D_b = D_v = 10$ and $K = 2$.

through a Hopf bifurcation whereas asynchronous instabilities occur through a zero-eigenvalue crossing. For both types of instabilities we can numerically calculate a threshold for D_v beyond which the particular instability is triggered. In Fig. 7 we plot the Hopf bifurcation threshold for a one-spike solution in the $D_b \rightarrow \infty$ limit for different values of $\tau_s \geq 0$, which illustrates the non-trivial dependence on the coupling parameter K and bulk-bound timescale constant τ_b . In particular, increasing the coupling strength K can both stabilize and destabilize the spike solution. By seeking parameter values for which (4.10) admits a zero-eigenvalue crossing for $1 \leq k \leq N - 1$, the numerically calculated asynchronous instability thresholds shown in Fig. 8 for select values of D_b illustrate that the coupling parameter also has a stabilizing or destabilizing effect with respect to the asynchronous instabilities for small and large values of K , respectively.

5. Dynamically Active Cells Coupled by Bulk Diffusion

We first formulate the coupled PDE-ODE bulk-cell model of [26] and [28], as inspired by [23]. In the 2-D bounded domain Ω with a reflecting boundary $\partial\Omega$ we assume that there are m dynamically active well-separated circular ‘‘cells’’ Ω_j of a common radius R_0 , centered at $\mathbf{X}_j \in \Omega$ for $j = 1, \dots, m$. In the bulk region $\Omega \setminus \cup_{j=1}^m \Omega_j$, the autoinducer $\mathcal{U}(\mathbf{X}, T)$ is assumed to satisfy

$$\mathcal{U}_T = D_B \Delta \mathcal{U} - k_B \mathcal{U}, \quad T > 0, \quad \mathbf{X} \in \Omega \setminus \cup_{j=1}^m \Omega_j; \quad \partial_{n_{\mathbf{X}}} \mathcal{U} = 0, \quad \mathbf{X} \in \partial\Omega; \quad (5.1a)$$

$$D_B \partial_{n_{\mathbf{X}}} \mathcal{U} = \beta_{1j} \mathcal{U} - \beta_{2j} \mu_j^1, \quad \mathbf{X} \in \partial\Omega_j, \quad j = 1, \dots, m, \quad (5.1b)$$

where $\partial_{n_{\mathbf{X}}}$ is the outer normal derivative pointing into the bulk region. The dimensional bulk diffusivity is $D_B > 0$, while $k_B > 0$ is the rate of degradation of the bulk signal. The Robin condition (5.1b) on the cell membrane, with permeabilities β_{1j} and β_{2j} , models the influx and efflux of one chemical species into and out of the j^{th} cell. The intracellular ODE kinetics \mathbf{F}_j for the n interacting species $\mu_j \equiv (\mu_j^1, \dots, \mu_j^n)^T$ within the j^{th} cell is coupled to the bulk region from an integration across the cell membrane. Defining $\mathbf{e}_1 \equiv (1, 0, \dots, 0)^T$, this coupling has the form

$$\frac{d\mu_j}{dT} = k_R \mu_c \mathbf{F}_j(\mu_j/\mu_c) + \mathbf{e}_1 \int_{\partial\Omega_j} (\beta_{1j} \mathcal{U} - \beta_{2j} \mu_j^1) dS_{\mathbf{X}}, \quad j = 1, \dots, m, \quad (5.1c)$$

where $k_R > 0$ is the dimensional intracellular reaction rate and $\mu_c > 0$ is a typical value for μ_j .

A key feature in this PDE-ODE model (5.1) is that only one signaling chemical, labelled by μ_j^1 , can permeate the j^{th} cell membrane with efflux parameter β_{2j} . This chemical communicates with spatially distant cells by diffusing through the bulk medium. The influx parameter β_{1j} controls the global feedback into the j^{th} cell from the bulk diffusion field generated by all the cells. A schematic diagram for the bulk-cell coupling is shown in Fig. 9 for $n = 2$ intracellular species.

In (5.1) it is assumed that the common radius R_0 of the cells is small in comparison to the domain length-scale L , and so we define $\varepsilon \equiv R_0/L \ll 1$. With the non-dimensionalization of (5.1)

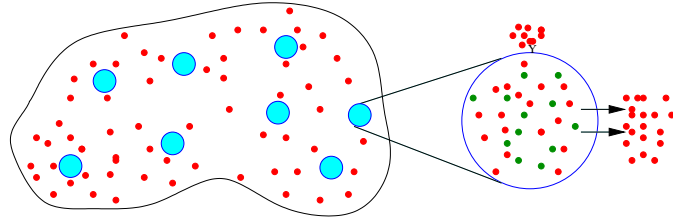


Figure 9: Dynamically active cells (in cyan) in a 2-D domain. The green and red dots represent the signaling chemicals in the cells, where only the red is secreted into the extracellular bulk region. Right: A zoom of the intracellular species, the secretion of signaling molecules into the bulk and the feedback into the cells.

as in [26] and [28], the dimensionless concentration $U(\mathbf{x}, t)$ in the bulk region satisfies

$$\tau \frac{\partial U}{\partial t} = D \Delta U - U, \quad t > 0, \quad \mathbf{x} \in \Omega \setminus \cup_{j=1}^m \Omega_{\varepsilon_j}; \quad \partial_n U = 0, \quad \mathbf{x} \in \partial\Omega; \quad (5.2a)$$

$$\varepsilon D \partial_n U = d_{1j} U - d_{2j} u_j^1, \quad \mathbf{x} \in \partial\Omega_{\varepsilon_j}, \quad j = 1, \dots, m, \quad (5.2b)$$

where $\Omega_{\varepsilon_j} \equiv \{\mathbf{x} \mid |\mathbf{x} - \mathbf{x}_j| \leq \varepsilon\}$. The bulk solution U is coupled to the intracellular dynamics by

$$\frac{d\mathbf{u}_j}{dt} = \mathbf{F}_j(\mathbf{u}_j) + \frac{\mathbf{e}_1}{\varepsilon\tau} \int_{\partial\Omega_{\varepsilon_j}} (d_{1j} U - d_{2j} u_j^1) ds, \quad j = 1, \dots, m. \quad (5.2c)$$

Here $\mathbf{u}_j \equiv (u_j^1, \dots, u_j^n)^T$ represents the n species in the j^{th} cell. The centers of the cells are assumed to be well-separated in the sense that $\text{dist}(\mathbf{x}_j, \mathbf{x}_k) = \mathcal{O}(1)$ for $j \neq k$ and $\text{dist}(\mathbf{x}_j, \partial\Omega) = \mathcal{O}(1)$ as $\varepsilon \rightarrow 0$. In (5.2), the key dimensionless parameters D , τ , d_{1j} , and d_{2j} are defined by

$$D \equiv \frac{D_B}{k_B L^2}, \quad \tau \equiv \frac{k_R}{k_B}, \quad d_{1j} \equiv \varepsilon \frac{\beta_{1j}}{k_B L} = \mathcal{O}(1), \quad d_{2j} \equiv \varepsilon \frac{\beta_{2j} L}{k_B} = \mathcal{O}(1). \quad (5.3)$$

For small values of the reaction-time parameter τ , the intracellular reactions proceed slowly relative to the time-scale of degradation of the bulk signal, and so little communication between the cells can occur. For large values of the effective bulk diffusivity D , the cells are readily able to synchronize their activities through the bulk medium and, in the well-mixed limit $D \rightarrow \infty$, the bulk signal becomes spatially homogeneous. In contrast, when D is small, communication between spatially distant cells is weak. In (5.3), the influx β_{1j} and efflux β_{2j} parameters are chosen as $\mathcal{O}(\varepsilon^{-1})$ so as to ensure that there is an $\mathcal{O}(1)$ transport across the membrane of the small cells.

5.1 Switch-like Onset of Intracellular Oscillations: A Hopf Bifurcation

By using strong localized perturbation theory [48] in the singularly perturbed limit $\varepsilon \rightarrow 0$, in [26] and [28] steady-state solutions for (5.2) were constructed and the linear stability problem was derived in the form of a nonlinear matrix eigenvalue problem. With Sel'kov intracellular kinetics, it was shown in [26] and [28] that switch-like intracellular oscillations can emerge via a Hopf bifurcation in parameter regimes where the cells, when uncoupled from the bulk medium, would otherwise only have a stable steady-state. The triggering of such diffusion-induced intracellular oscillations, for a specific permeability set and a given spatial configuration of cells, is encapsulated in a phase diagram in the τ versus D parameter space. We now briefly summarize this theory of [26] and [28] and we provide two new results illustrating the theory.

Sel'kov intracellular kinetics, used as a conceptual model of glycolysis oscillations (cf. [30], [49]), involves two intracellular species $\mathbf{u}_j = (u_j^1, u_j^2)^T$, and is given by

$$\mathbf{F}_j = (F_{j1}, F_{j2})^T; \quad F_{j1} \equiv \alpha_j u_j^2 + u_j^2 (u_j^1)^2 - u_j^1, \quad F_{j2} \equiv \zeta_j \left(\mu_j - \left[\alpha_j u_j^2 + u_j^2 (u_j^1)^2 \right] \right). \quad (5.4)$$

We fix $\mu_j \equiv \mu = 2$ and $\zeta_j \equiv \zeta = 0.15$ for all cells, and choose α_j large enough so that an isolated cell with no influx (i.e. $d_{1j} = 0$) has only a linearly stable rest state. With no influx, (5.2c) has the dynamics $du_j/dt = \mathbf{F}_j(\mathbf{u}_j) - 2\pi d_{2j} u_j^1 \mathbf{e}_1 / \tau$ where \mathbf{F}_j is given in (5.4). This ODE system has only a linearly stable steady state and no limit cycle oscillations when (see Fig. 2 of [28])

$$\alpha_j > -\frac{\mu_j^2}{\chi_j^2} + \frac{1}{2\zeta_j} \left[-\chi_j + \sqrt{\chi_j^2 + \frac{8\zeta_j \mu_j^2}{\chi_j}} \right], \quad \text{with} \quad \chi_j \equiv 1 + \frac{2\pi d_{2j}}{\tau}, \quad (5.5)$$

where $\mu_j = 2$ and $\zeta_j = 0.15$. In this way, intracellular oscillations that occur below in various regions of the (D, τ) plane arise only by the diffusive coupling of the cells through the bulk.

With Sel'kov kinetics (5.4), it was shown in §2 of [28] that for $\varepsilon \rightarrow 0$ there is a unique steady-state solution to (5.2). In the outer region, where $|\mathbf{x} - \mathbf{x}_j| \gg \mathcal{O}(\varepsilon)$, the steady-state bulk solution for $\varepsilon \rightarrow 0$ is $U \sim -2\pi \sum_{i=1}^m A_i G_0(\mathbf{x}; \mathbf{x}_i)$, where $\mathcal{A} \equiv (A_1, \dots, A_m)^T$ solves the linear system

$$\left(I + 2\pi\nu\mathcal{G}_0 + \nu D P_1 + \frac{2\pi\nu D}{\tau} P_2 \right) \mathcal{A} = -\mu\nu P_2 \mathbf{e}. \quad (5.6)$$

Here $\nu \equiv -1/\log \varepsilon$, $P_1 \equiv \text{diag}(1/d_{11}, \dots, 1/d_{1m})$, $P_2 \equiv \text{diag}(d_{21}/d_{11}, \dots, d_{2m}/d_{1m})$, and $\mathbf{e} \equiv (1, \dots, 1)^T$. In the limit $\varepsilon \rightarrow 0$ it was shown in §2 of [28] that all of the discrete eigenvalues of the linearization of this steady-state are contained in the set $\Lambda(\mathcal{M})$, defined by

$$\Lambda(\mathcal{M}) \equiv \{\lambda \mid \det \mathcal{M}(\lambda) = 0\}, \quad \text{where} \quad \mathcal{M}(\lambda) \equiv I + 2\pi\nu\mathcal{G}_\lambda + \nu D P_1 + \frac{2\pi\nu D}{\tau} P_2 \mathcal{K}. \quad (5.7)$$

We refer to (5.7) as the globally coupled eigenvalue problem (GCEP). In (5.6) and (5.7), \mathcal{G}_λ is the symmetric reduced-wave Green's matrix, with entries $(\mathcal{G}_\lambda)_{ij} \equiv G_\lambda(\mathbf{x}_i; \mathbf{x}_j)$ for $i \neq j$ and $(\mathcal{G}_\lambda)_{jj} \equiv R_\lambda(\mathbf{x}_j)$, where $G_\lambda(\mathbf{x}; \mathbf{x}_j)$ is the Green's function, with regular part $R_\lambda(\mathbf{x}_j)$, satisfying

$$\begin{aligned} \Delta G_\lambda - \frac{(1 + \tau\lambda)}{D} G_\lambda &= -\delta(\mathbf{x} - \mathbf{x}_j), \quad \mathbf{x} \in \Omega; \quad \partial_n G_\lambda = 0, \quad \mathbf{x} \in \partial\Omega; \\ G_\lambda(\mathbf{x}; \mathbf{x}_j) &\sim -\frac{1}{2\pi} \log |\mathbf{x} - \mathbf{x}_j| + R_\lambda(\mathbf{x}_j) + o(1), \quad \text{as} \quad \mathbf{x} \rightarrow \mathbf{x}_j. \end{aligned} \quad (5.8)$$

In (5.7), the diagonal matrix \mathcal{K} has entries $(\mathcal{K})_{jj} = (\lambda + \det J_j) / (\lambda^2 - \lambda \text{tr} J_j + \det J_j)$, where J_j is the Jacobian of the Sel'kov kinetics \mathbf{F}_j at the steady-state.

The GCEP (5.7) depends on D , τ , the permeabilities d_{1j} and d_{2j} , for $j = 1, \dots, m$, as encoded in the matrices P_1 and P_2 , and the spatial configuration $\{\mathbf{x}_1, \dots, \mathbf{x}_m\}$ of the cell centers within Ω encoded in the Green's matrix \mathcal{G}_λ . We remark that the diagonal matrix \mathcal{K} in (5.7) also depends on all of these parameters through the steady-state solution. When Ω is the unit disk the Green's matrix \mathcal{G}_λ can be calculated analytically (cf. [28]). Any element $\lambda \in \Lambda(\mathcal{M})$ for which $\Re(\lambda) > 0$ provides an approximation, valid as $\varepsilon \rightarrow 0$, for an unstable discrete eigenvalue of the linearization of the steady-state. Hopf bifurcation (HB) boundaries can be calculated by ensuring that the eigenvalue with the largest real part satisfies $\det \mathcal{M}(i\lambda_I) = 0$.

Our first example, not considered in [28], is for a ring and center cell pattern in the unit disk that consists of four equally-spaced cells on a ring of radius r_0 concentric within the unit disk with an additional cell at the center of the disk. In Fig. 10a we plot a HB boundary in the (D, τ) plane for a few ring radii r_0 when the cells are all identical. Synchronous intracellular oscillations for the cells on the ring are predicted inside the lobes shown in Fig. 10a. However, as shown in Fig. 10b, by decreasing the Sel'kov parameter α for the center cell to be closer to the stability boundary in (5.5) for an isolated cell, this single "defective" center cell triggers intracellular oscillations for the entire collection of cells in a larger region of the (D, τ) parameter space. These theoretical predictions are confirmed in the lower row of Fig. 10 where we show full numerical results for the intracellular component u_1 for the center cell and the synchronous ring cells, as computed numerically from the bulk-cell PDE-ODE system (5.2) using FlexPDE [50]. For the choice of parameters in the caption of Fig. 10, we observe that the lobes of instability in the (D, τ) parameter space are bounded. Qualitatively, with only five cells, as D becomes too large the bulk signal is

rapidly washed away from each cell, and there is an insufficient diffusive gradient near the cells to trigger collective oscillations.

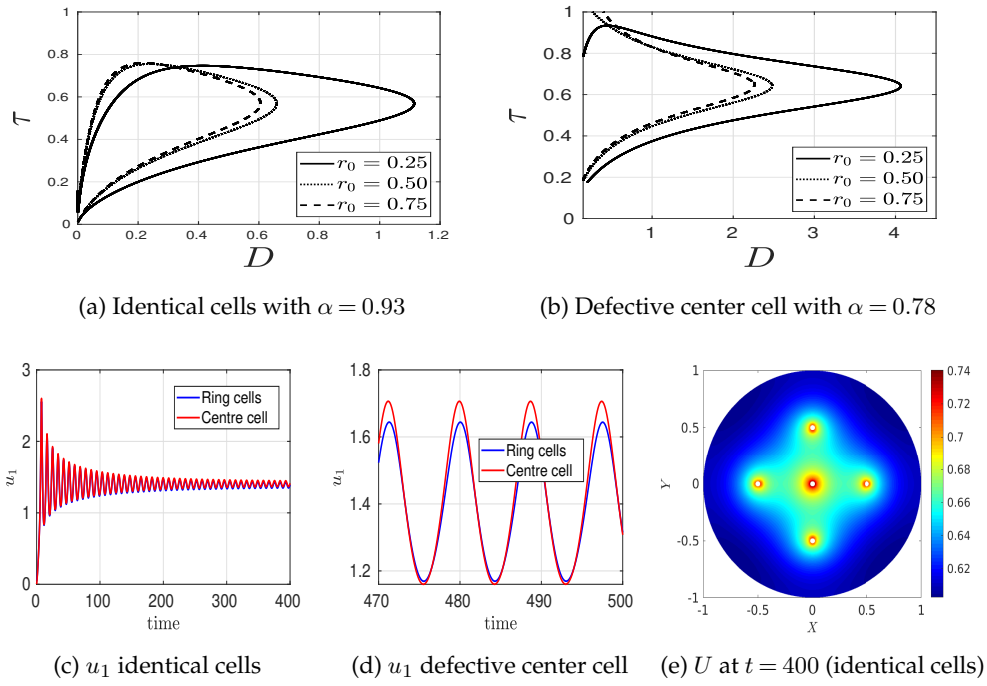


Figure 10: Top row: HB boundaries in the (D, τ) plane for a pattern of four equally-spaced cells on a ring of radius r_0 with an additional cell at the center. Top left: identical cells with $\alpha = 0.93$. Top right: now $\alpha = 0.78$ for center cell. Bottom row: FlexPDE [50] results computed from (5.2) for the intracellular component u_1 and the bulk solution U when $r_0 = 0.5$, $D = 2$, and $\tau = 0.65$. Bottom left: identical cells with $\alpha = 0.9$ showing decaying oscillations. Bottom middle: defective center cell has $\alpha = 0.78$ and sustained oscillations occur. Bottom right: contour plot of U at $t = 400$ for identical cells. Parameters: $\varepsilon = 0.02$, $\mu = 2$, $\zeta = 0.15$, $d_1 = 0.3$, and $d_2 = 0.2$.

In our second example, not considered in [28], we take $m = 50$ non-overlapping cells of radii $\varepsilon = 0.02$ that are randomly distributed in the unit disk and have identical Sel'kov kinetic parameters and a common efflux parameter d_2 . The cell pattern is shown in Fig. 11b. We consider the large D regime, given by $D = D_0/\nu$ with $D_0 = \mathcal{O}(1)$ and $\nu = -1/\log \varepsilon \ll 1$, where the challenging problem of finding roots to $\det \mathcal{M}(i\lambda_I) = 0$ can be reduced asymptotically to the much simpler scalar problem of determining a zero-crossing for one specific matrix eigenvalue σ of $\mathcal{M}\mathbf{e} = \sigma\mathbf{e}$ (see Proposition 5 of [28]). By exploiting this simplification, in Fig. 11a we plot a numerically computed HB boundary in the (τ, D_0) plane when the cells have a common influx parameter $d_1 = 0.8$ and when the influx parameter is uniformly distributed on $0.4 \leq d_1 \leq 0.8$, but where two cells are assigned the bounds of this interval in d_1 . From Fig. 11a we observe that when cell heterogeneity is introduced through the influx permeability there is a narrower range of τ where intracellular oscillations occur. From the unbounded regions in Fig. 11a we observe, in contrast to the situation shown in Fig. 10 for the ring and center cell pattern, that intracellular oscillations will occur in the well-mixed limit $D_0 \rightarrow \infty$. Although the spatial gradient of the bulk signal is very weak when $D_0 \gg 1$, the presence of a large number of cells can sufficiently increase the (roughly) spatially uniform level of the bulk signal so as to trigger collective oscillations of the entire group of cells. This qualitative behavior is known as quorum-sensing (see [28] and

the references therein), and its occurrence depends primarily on the number of cells and the cell membrane permeabilities.

As shown in §3 of [28], an additional simplification for the large bulk diffusivity distinguished limit $D = D_0/\nu \gg 1$, is that the time-dependent solution to the bulk-cell PDE-ODE model (5.2) can be approximated by the following $nm + 1$ dimensional ODE-DAE system for $\bar{U} \approx |\Omega|^{-1} \int_{\Omega} U dx$ and the intracellular species (see Proposition 2 of [28]):

$$\frac{d\bar{U}}{dt} = -\frac{1}{\tau}\bar{U} - \frac{2\pi D_0}{\tau|\Omega|} \mathbf{e}^T \mathbf{b}; \quad \frac{d\mathbf{u}_j}{dt} = \mathbf{F}_j(\mathbf{u}_j) + \frac{2\pi D_0 \mathbf{e}_1}{\tau} b_j, \quad j = 1, \dots, m, \quad (5.9a)$$

where $\mathbf{e} \equiv (1, \dots, 1)^T$, $\mathbf{e}_1 \equiv (1, 0, \dots, 0)^T$ and $\mathbf{b} \equiv (b_1, \dots, b_m)^T$ solves the linear algebraic system

$$(I + D_0 P_1 + 2\pi\nu \mathcal{G}_N) \mathbf{b} = \bar{U} \mathbf{e} - P_2 \mathbf{u}^1, \quad (5.9b)$$

where $\mathbf{u}^1 \equiv (u_1^1, \dots, u_m^1)^T$. Here \mathcal{G}_N is the Neumann Green's matrix with entries $(\mathcal{G}_N)_{ij} \equiv G_N(\mathbf{x}_i; \mathbf{x}_j)$ for $i \neq j$ and $(\mathcal{G}_N)_{jj} \equiv R_N(\mathbf{x}_j)$, where $G_N(\mathbf{x}; \mathbf{x}_j)$, with regular part $R_N(\mathbf{x}_j)$, satisfies

$$\Delta G_N = \frac{1}{|\Omega|} - \delta(\mathbf{x} - \mathbf{x}_j), \quad \mathbf{x} \in \Omega; \quad \partial_n G_N = 0, \quad \mathbf{x} \in \partial\Omega; \quad (5.10a)$$

$$G_N(\mathbf{x}; \mathbf{x}_j) \sim -\frac{1}{2\pi} \log |\mathbf{x} - \mathbf{x}_j| + R_N(\mathbf{x}_j) + o(1), \quad \text{as } \mathbf{x} \rightarrow \mathbf{x}_j; \quad \int_{\Omega} G_N dx = 0. \quad (5.10b)$$

By using the explicit formula for G_N for the unit disk (cf. [28]), the ODE-DAE system (5.9) is solved numerically for Sel'kov kinetics at the three labelled points in the phase diagram of Fig. 11a for the case where the cells are heterogeneous due to the random influx parameter d_1 . The results shown in Fig. 12 for three specific cells confirm the theoretical prediction based on Fig. 11a.

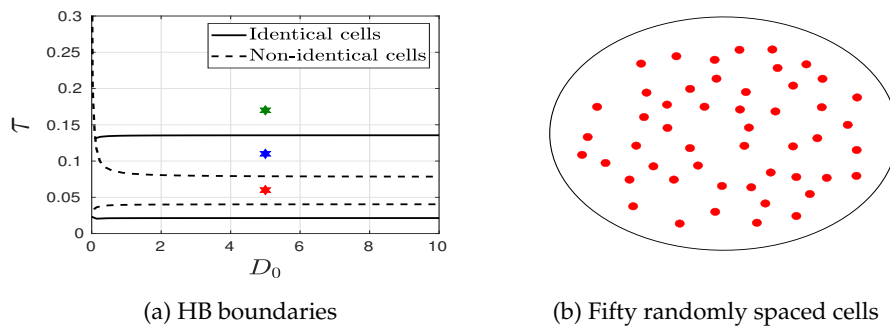


Figure 11: Left: HB boundaries in the (D_0, τ) plane for $m = 50$ randomly placed cells in the unit disk. Heavy solid: identical cells with $d_1 = 0.8$. Dashed: Each cell has an influx parameter d_1 uniformly distributed on $0.4 \leq d_1 \leq 0.8$. Right: spatial pattern of $m = 50$ cells. Parameters: $d_2 = 0.2$, $\varepsilon = 0.02$, $\alpha = 0.9$, $\mu = 2$, $\zeta = 0.15$.

6. Discussion

The wide variety of specific cell signalling problems that involve the binding of surface receptors (cf. [1–4, 11, 12, 14, 15]), has provided a recent impetus for studying pattern-forming properties associated with novel classes of RD systems that involve the coupling of a linear RD system in the interior of a multi-dimensional domain to nonlinear diffusive processes that occur in a thin strip that protrudes from the domain boundary. In this context, the bulk-membrane system derived in (2.8) of §2 arises from the asymptotic limit of a vanishing width of this thin strip, together with a certain scaling law for the membrane-bound species. However, the analysis of pattern forming properties for this reduced system (2.8) is still rather challenging owing, not only

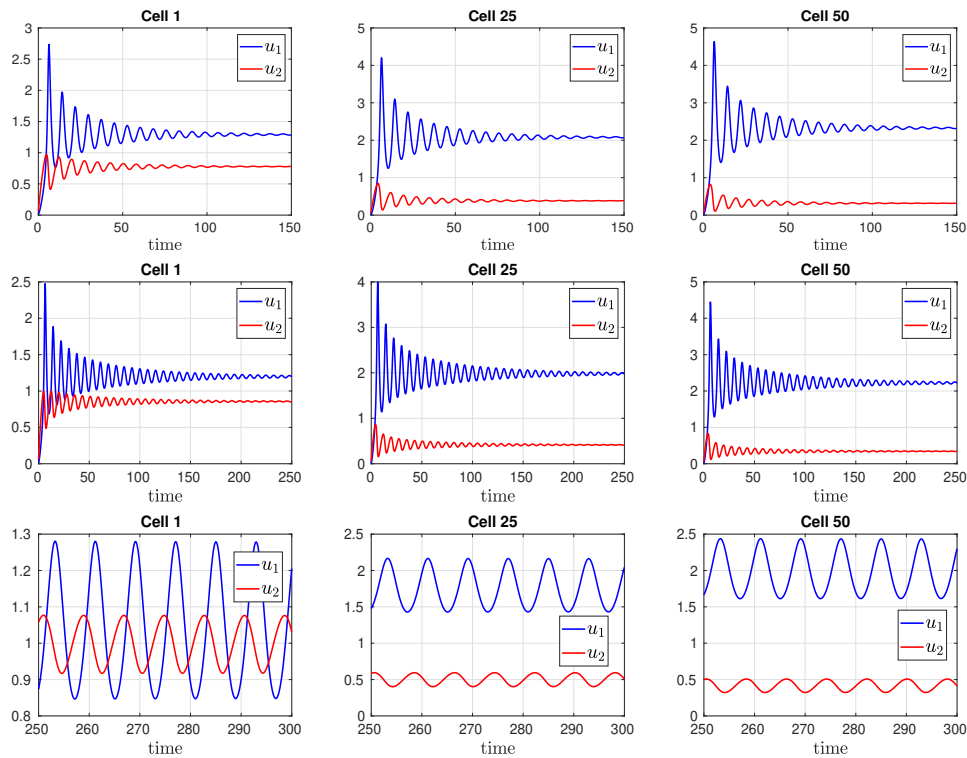


Figure 12: Intracellular components u_1 and u_2 versus time for three cells, as computed from the ODE-DAE system (5.9), at the green star (top row) $(D, \tau) = (5, 0.06)$, blue star (middle row) $(D, \tau) = (5, 0.11)$, and red star (lower row) $(D, \tau) = (5, 0.17)$ labelled points in the HB diagram of Fig. 11a. Cells have random influx parameters d_1 on $0.4 \leq d_1 \leq 0.8$, but where cells 1 and 50 are assigned $d_1 = 0.4$ and $d_1 = 0.8$, respectively. Left column: Cell 1 with $d_1 = 0.4$ and $\mathbf{x}_1 = (0.765, -0.141)$. Middle column: Cell 25 with $d_1 = 0.7086$ and $\mathbf{x}_{25} = (-0.3223, 0.0489)$. Right column: Cell 50 with $d_1 = 0.8$ and $\mathbf{x}_{50} = (0.763, -0.362)$. Other parameters as in Fig. 11. As predicted, among these three points, sustained intracellular oscillations occur only at the red star in Fig. 11a.

to the complexity of the geometry, but also from the fact that steady-state solutions are in general not spatially uniform, even in radially symmetric domains. As a result, this prohibits applying a standard Turing-type linear stability analysis that has been used so successfully to analyze pattern formation in more conventional RD systems where spatially uniform steady-states often occur.

For a coupled bulk-membrane RD system on a circular bulk domain, in §3.1 we have outlined the analysis in [21] for the construction of radially symmetric spatially non-uniform steady-states and the derivation of amplitude equations characterizing the weakly nonlinear dynamics of spatio-temporal patterns near Hopf and pitchfork bifurcation points associated with the linearization of this non-uniform base state. By assuming equal diffusion rates for the membrane-bound species, our results have shown that the coupling via a passive bulk diffusion process can provide an alternative destabilizing mechanism in comparison to the usual diffusion-driven instability paradigm. Although we have only illustrated the weakly nonlinear analysis of [21] for the Brusselator kinetics, the normal form analysis of [21] can be readily implemented for an arbitrary reaction kinetics on the boundary of a disk. In §3.2, we have numerically explored the formation of rotating waves in the highly nonlinear regime, away from $O(2)$ symmetric Hopf bifurcations. These rotating wave solutions are not amenable to study through a weakly nonlinear analysis as they originate from a secondary instability, behind the "trivial" Hopf bifurcation associated with radially symmetric oscillations. However, the situation is rather different for

models where the total concentration of species is assumed to remain constant, which is a usual hypothesis of cell polarization models in both standard [51,52] and bulk-membrane [2–4] versions. In a recent study on a mass-conserved bulk-membrane RD for intracellular oscillations and polarization [21], which also assumed circular bulk geometry, a rather wide parameter regime was found that allowed the formation of rotating and standing waves as primary instabilities. This was observed as a direct consequence of mass conservation, selecting spatial modes which naturally redistribute the total mass of species, thereby excluding the trivial (radially symmetric) mode. Hence, it would be worthwhile to extend the weakly nonlinear theory of [21], as outlined in §3.1, to the case of $O(2)$ symmetric Hopf bifurcations in mass-conserved bulk-membrane RD models with periodic boundary conditions. In doing so, the interactions of rotating and standing waves near onset and their stability properties can be analyzed. For this task, the normal form classification from [40] will be particularly useful. In another direction it would be worthwhile to extend the weakly nonlinear theory of [21] to realistic geometries in 2-D and 3-D such as ellipses, cylinders, spheres, and ellipsoids.

For a bulk-membrane RD system with GM membrane kinetics on the boundary of a 2-D disk, we have highlighted some results in [22] for the existence and linear stability of localized membrane-bound spike patterns. Although the analysis in §4 was presented only for a specific choice of the exponents of the nonlinear terms in the GM model, for which the stability analysis can be simplified, the analysis in [22] was done more generally. We anticipate that a similar analysis in a 2-D disk can be done for other membrane kinetics such as the Schnakenberg model. One main challenge, however, is to analyze similar bulk-membrane problems in a 3-D setting, whereby localized spot patterns occur on the boundary of a spherical domain. In this 3-D context, it would be interesting to determine how a spatially inhomogeneous production of signalling chemicals inside the domain can influence the location where stable localized structures can be formed on the domain boundary. Finally, more elaborate bulk-membrane models involving time-dependent domain growth due to either chemical signalling or mechanical stresses pose considerable challenges for an analytical characterization of pattern formation properties.

For the bulk-cell PDE-ODE system (5.2), the use of Sel'kov intracellular dynamics has provided a clear conceptual model for the sudden emergence, owing to a Hopf bifurcation, of intracellular oscillations as mediated by an autoinducer field. In the absence of bulk coupling, the Sel'kov ODE dynamics is an example of a conditional oscillator, in that the kinetics parameters can be tuned to be relatively close to the critical values where limit cycle oscillations can occur. The introduction of cell-cell coupling through the bulk diffusion field can then effectively change the marginal stability boundary, leading to the emergence of intracellular oscillations. Intracellular oscillations have also been observed in several specific biological systems (cf. [32], [33], [34]). From the viewpoint of applications, it would be interesting to analyze (5.1) for intracellular kinetics that are based on detailed biologically realistic models of signaling pathways, such as those of [53] and [54] for glycolytic oscillations. We remark that the bulk-cell model (5.2) readily allows for including any parameter values, such as kinetic rate constants and cell membrane permeabilities, that can be extracted from biological measurements. Extensions of the analysis of the 2-D model (5.2) to either a 3-D setting, or to allow for two bulk diffusion fields, should be undertaken.

One challenging open numerical issue in the analysis of bulk-cell models concerns developing well-conditioned numerical techniques to implement the linear stability analysis based on the root-finding condition $\det(\mathcal{M}(\lambda)) = 0$ for the GCEP given in (5.7) for a large number of randomly placed cells with arbitrary permeabilities. Solution strategies for such nonlinear matrix eigenvalue problems are typically restricted to matrices with special structure, such as Hermitian matrices, matrices with low-rank dependence on λ , or matrices that are quadratic or rational in λ (cf. [55]).

Data Accessibility. The precise cell locations and influx parameters d_{1j} used for Fig. 11b are tabulated.

Authors' Contributions. All authors contributed equally to this article.

Competing Interests. There are no competing interests.

Funding. D. Gomez was supported by a NSERC CGS-D. F. Paquin-Lefebvre was supported by a UBC four-year doctoral fellowship. M. Ward was supported by the NSERC Discovery Grant Program.

Acknowledgements. The authors gratefully acknowledge the contributions of our colleagues Prof. Wayne Nagata and Prof. Juncheng Wei of UBC to some of the work surveyed herein, as well as Prof. Hannes Uecker from the University of Oldenburg for helpful discussions on *pde2path*.

References

1. Levine H, Rappel WJ. 2005 Membrane-bound Turing patterns. *Phys. Rev. E* **72**, 061912.
2. Rätz A, Röger M. 2012 Turing instabilities in a mathematical model for signaling networks. *J. Math. Biol.* **65**, 1215–1244.
3. Diegmiller R, Montanelli H, Muratov CB, Shvartsman SY. 2018 Spherical caps in cell polarization. *Biophys. J.* **115**, 26–30.
4. Cusceddu D, Edelstein-Keshet L, Mackenzie J, Portet S, Madzvamuse A. 2019 A coupled bulk-surface model for cell polarisation. *J. Theor. Biol.* **481**, 119 – 135.
5. Paquin-Lefebvre F, Xu B, DiPietro KL, Lindsay AE, Jilkin A. 2020 Pattern formation in a coupled membrane-bulk reaction-diffusion model for intracellular polarization and oscillations. *J. Theor. Biol.* **497**, 110242, 23.
6. Rappel WJ, Edelstein-Keshet L. 2017 Mechanisms of cell polarization. *Current Opinion in Systems Biology* **3**, 43–53.
7. Huang KC, Meir Y, Wingreen NS. 2003 Dynamic structures in Escherichia coli: spontaneous formation of MinE rings and MinD polar zones. *PNAS* **100**, 12724–12728.
8. Sherratt DJ. 2016 Oscillation helps to get division right. *PNAS* **113**, 2803–2805.
9. Das M, Drake T, Wiley DJ, Buchwald P, Vavylonis D, Verde F. 2012 Oscillatory dynamics of Cdc42 GTPase in the control of polarized growth. *Science* **337**, 239–243.
10. Howard M, Rutenberg AD, de Vet S. 2001 Dynamic compartmentalization of bacteria: Accurate division in E. Coli. *Phys. Rev. Lett.* **87**, 278102.
11. Halatek J, Frey E. 2012 Highly canalized MinD transfer and MinE sequestration explain the origin of robust MinCDE-protein dynamics. *Cell reports* **1**, 741–752.
12. Bonny M, Fischer-Friedrich E, Loose M, Schwille P, Kruse K. 2013 Membrane binding of MinE allows for a comprehensive description of Min-protein pattern formation. *PLoS Computational Biology* **9**, e1003347.
13. Stolerman LM, Getz M, Llewellyn Smith S, Holst M, Rangamani P. 2020 Stability analysis of a bulk-surface reaction model for membrane protein clustering. *Bulletin of mathematical biology* **82**.
14. Madzvamuse A, Chung AHW, Venkataraman C. 2015 Stability analysis and simulations of coupled bulk-surface reaction-diffusion systems. *Proc. R. Soc., Ser. A* **471**, 20140546, 18.
15. Madzvamuse A, Chung AHW. 2016 The bulk-surface finite element method for reaction-diffusion systems on stationary volumes. *Finite Elem. Anal. Design* **108**, 9 – 21.
16. Elliott CM, Ranner T, Venkataraman C. 2017 Coupled bulk-surface free boundary problems arising from a mathematical model of receptor-ligand dynamics. *SIAM J. Appl. Math.* **49**, 369–397.
17. Giese W, Eigel M, Westerheide S, Engwer C, Klipp E. 2015 Influence of cell shape, inhomogeneities and diffusion barriers in cell polarization models. *Physical Biology* **12**, 066014.
18. Hausberg S, Röger M. 2018 Well-posedness and fast-diffusion limit for a bulk-surface reaction-diffusion system. *NoDEA Nonl. Diff. Eq. Appl.* **25**, Paper No. 17, 32.
19. Niethammer B, Röger M, Velázquez JLL. 2020 A bulk-surface reaction-diffusion system for cell polarization. *Interfaces Free Bound.* **22**, 85–117.
20. Disser K. 2020 Global existence, uniqueness and stability for nonlinear dissipative bulk-interface interaction systems. *Journal of Differential Equations* **269**, 4023–4044.
21. Paquin-Lefebvre F, Nagata W, Ward MJ. 2019 Pattern formation and oscillatory dynamics in a two-dimensional coupled bulk-surface reaction-diffusion system. *SIAM J. Appl. Dyn. Syst.* **18**, 1334–1390.
22. Gomez D, Ward MJ, Wei J. 2019 The linear stability of symmetric spike patterns for a bulk-membrane coupled Gierer-Meinhardt model. *SIAM J. Appl. Dyn. Syst.* **18**, 729–768.
23. Müller J, Kuttler C, Hense BA, Rothballer M, Hartmann A. 2006 Cell-cell communication by quorum sensing and dimension-reduction. *J. Math. Bio.* **53**, 672–702.
24. Müller J, Uecker H. 2013 Approximating the dynamics of communicating cells in a diffusive medium by ODEs – homogenization with localization. *J. Math. Bio.* **67**, 1023–1065.
25. Uecker H, Müller J, Hense BA. 2014 Individual-based model for quorum sensing with background flow. *Bulletin of mathematical biology* **76**, 1727–1746.

26. Gou J, Ward MJ. 2016 An asymptotic analysis of a 2-D model of dynamically active compartments coupled by bulk diffusion. *J. Nonlin. Sci.* **26**, 979–1029.
27. Iyaniwura S, Ward MJ. 2020 Localized signaling compartments in 2-D coupled by a bulk diffusion field: quorum sensing and synchronous oscillations in the well-mixed limit. *Europ. J. Appl. Math.* pp. 1–31. doi:10.1017/S0956792520000261.
28. Iyaniwura S, Ward MJ. 2021 Synchrony and oscillatory dynamics for a 2-D PDE-ODE model of diffusion-sensing with small signaling compartments. *SIAM J. Appl. Dyn. Sys.* **20**, 438–499.
29. Gregor T, Fujimoto K, Masaki N, Sawai S. 2010 The onset of collective behavior in social amoebae. *Science* **328**, 1021–1025.
30. Nanjundiah V. 1998 Cyclic AMP oscillations in Dictyostelium Discoideum: Models and observations. *Biophys. Chem.* **72**, 1–8.
31. Goldbeter A. 1997 *Biochemical oscillations and cellular rhythms: the molecular bases of periodic and chaotic behaviour*. Cambridge university press.
32. Danø S, Madsen MF, Sørensen PG. 2007 Quantitative characterization of cell synchronization in yeast. *PNAS* **104**, 12732–12736.
33. Danø S, Sørensen PG, Hynne F. 1999 Sustained oscillations in living cells. *Nature* **402**, 320–322.
34. De Monte S, d’Ovidio F, Danø S, Sørensen PG. 2007 Dynamical quorum sensing: Population density encoded in cellular dynamics. *PNAS* **104**, 18377–18381.
35. Shinomoto S, Kuramoto Y. 1986 Phase transitions in active rotator systems. *Progress of Theoretical Physics* **75**, 1105–1110.
36. Uecker H, Wetzell D, Rademacher JDM. 2014 pde2path—a Matlab package for continuation and bifurcation in 2D elliptic systems. *Numer. Math. Theory Methods Appl.* **7**, 58–106.
37. Uecker H. 2020 Pattern formation with pde2path – a tutorial. <https://arxiv.org/abs/1908.05211>.
38. Cross MC, Hohenberg PC. 1993 Pattern formation outside of equilibrium. *Rev. Mod. Phys.* **65**, 851–1112.
39. Walgraef D. 1997 *Spatio-temporal Pattern Formation vol. 2 Partially Ordered Systems*. Springer-Verlag, New York.
40. van Gils SA, Mallet-Paret J. 1986 Hopf bifurcation and symmetry: travelling and standing waves on the circle. *Proc. Roy. Soc. Edinburgh Sect. A* **104**, 279–307.
41. Uecker H. 2019 Hopf bifurcation and time periodic orbits with pde2path—algorithms and applications. *Commun. Comput. Phys.* **25**, 812–852.
42. Gierer A, Meinhardt H. 1972 A theory of biological pattern formation. *Kybernetik* **12**, 30–39.
43. Wei J. 1999 On single interior spike solutions of the Gierer-Meinhardt system: uniqueness and spectrum estimates. *Europ. J. Appl. Math.* **10**, 353–378.
44. Iron D, Ward MJ, Wei J. 2001 The stability of spike solutions to the one-dimensional Gierer-Meinhardt model. *Phys. D* **150**, 25–62.
45. Ward MJ, Wei J. 2003 Hopf bifurcation and oscillatory instabilities of spike solutions for the one-dimensional Gierer-Meinhardt model. *J. Nonlin. Sci.* **13**, 209–264.
46. Wei J, Winter M. 2007 Existence, classification and stability analysis of multiple-peaked solutions for the Gierer-Meinhardt system in \mathbf{R}^1 . *Methods Appl. Anal.* **14**, 119–163.
47. Moyles I, Tse WH, Ward MJ. 2016 On explicitly solvable nonlocal eigenvalue problems and the stability of localized stripes in reaction-diffusion systems. *Studies in Appl. Math.* **136**, 89–136.
48. Ward MJ. 2018 Spots, traps, and patches: Asymptotic analysis of localized solutions to some linear and nonlinear diffusive systems. *Nonlinearity* **31**, R189.
49. Sel’kov EE. 1968 Self-Oscillations in Glycolysis 1. A Simple Kinetic Model. *Europ. J. Biochem.* **4**, 79–86.
50. FlexPDE. 2015 *PDE Solutions inc*. Available at <http://www.pdesolutions.com>.
51. Mori Y, Jilkine A, Edelstein-Keshet L. 2011 Asymptotic and bifurcation analysis of wave-pinning in a reaction-diffusion model for cell polarization. *SIAM J. Appl. Math.* **71**, 1401–1427.
52. Jilkine A, Edelstein-Keshet L. 2011 A comparison of mathematical models for polarization of single eukaryotic cells in response to guided cues. *PLoS Computational Biology* **7**, e1001121.
53. Wolf J, Heinrich R. 2000 Effect of cellular interaction on glycolytic oscillations in yeast: a theoretical investigation. *Biochem J.* **345**, 321–334.
54. Henson MA, D. M, Reuss M. 2002 Cell population modelling of yeast glycolytic oscillations. *Biochem J.* **368**, 433–446.
55. Güttel S, Tisseur F. 2017 The Nonlinear Eigenvalue Problem. *Acta Numerica* **26**, 1–94.